Nanoscale

ROYAL SOCIETY OF CHEMISTRY

PAPER

View Article Online
View Journal | View Issue

Cite this: *Nanoscale*, 2025, **17**, 24699

Orthogonal design and dual-mode construction of oriented bundles of fluorapatite from organic fibrils in shark enameloid

Shiho Akimoto, Yuya Oaki and Hiroaki Imai *

The structural design and formation processes of bundled structures consisting of *c*-axis-oriented fluorapatite (FA) fibers were studied to clarify the hierarchical architecture in the tooth enameloid of sharks in the Lamnidae family. Here, we focused on the orthogonal configuration of radial bundles (RBs) and parallel bundles (PBs) in the outer layer. From multidirectional characterization of mature and immature teeth, RBs and PBs were found to be constructed through different modes from collagen and non-collagenous organic fibrils, respectively. In the previous stage of calcification (stage 0), collagen bundles are produced as platy bands bridging from the dentin to the tooth surface, and then the non-collagenous fibrils are arranged perpendicularly to the bundles. In stage 1, the FA fibers of PBs are formed with the gradual transformation of non-collagenous fibrils with the infiltration of calcium and phosphate ions (Mode NC). In stage 2, RBs calcify through the crystal growth of FA fibers along with collagen fibrils that disappear gradually (Mode C). In stage 3, the orthogonal architecture matures through the widening of the FA fibers of RBs and decreasing organic matter. The FA bundles in other parts of the enameloid were deduced to be constructed from non-collagenous fibrils through Mode NC. Dual-mode construction is essential for the structural design of the sophisticated architecture consisting of crystal bundles with controlled directions.

Received 25th August 2025,
Accepted 30th September 2025

DOI: 10.1039/d5nr03589a

rsc.li/nanoscale

Introduction

Biological minerals, such as shells and bones, are composite materials made of inorganic and organic components produced by living organisms.[1–4] The sophisticated architectures of various shells and teeth have defensive and offensive uses, respectively. The hierarchical structures are produced through biomineralization processes under ambient aqueous conditions where the polymorph, size, and shape of crystal building blocks of biominerals are controlled by biogenic organic molecules.[4–9] Clarifying biogenic architectures and their formation processes is important for developing environmentally friendly technologies for the biomimetic production of novel functional materials consisting of calcium-based minerals.[10–12]

Of the biomineral family, the enamel and the enameloid—the outer layers of teeth—are regarded as the hardest tissues in the bodies of organisms. Their specific nature is ascribed to adequately bundled structures in which hydroxyapatite, carbonate apatite, and fluorapatite (FA) are organized with a small fraction of organic components.[13–21] The fibrous apatite crystals in one bundle are oriented at relatively high angles to adjacent bundles. In general, the complex hierarchical structures are closely related to the strength of organic–inorganic composites.[4,11,12] The enameloid, the hard outer tissue of fish teeth, is distinct from the enamel in mammals because their embryological processes are quite different.[22,23] As compared the enamel,[13,14,16,17,24–26] compartmented variations in the detailed structures and construction routes of the enameloid have not been sufficiently studied at macro- and micro-scales.[18–23,27–33] Shark tooth enameloid is known to exhibit extremely high strength.[20] The tough and hard properties and various unique characteristics are different from those of the enamel. Moreover, sharks are polyphyodonts, whose teeth are continually replaced throughout their lives.[34,35] Since immature teeth are prepared behind the mature ones on the jaw bone (Fig. S1 in the SI), we can study the process of tooth formation. Clarifying the structural design and the formation routes of shark enameloid should be helpful for developing novel light weight high-strength materials.

In this study, we investigated the hierarchical architecture and the formation processes of apatite bundles of the tooth enameloid of sharks in the Lamnidae family. We used two Lamnidae species (*Isurus oxyrinchus* and *Lamna ditropis*). Most data were obtained using samples from adult *Isurus oxyrinchus* individuals. Here, we confirmed that the tooth shape and microstructure of *Isurus oxyrinchus* and *Lamna ditropis* were almost the same. TEM images of the organic matrix before cal-

Department of Applied Chemistry, Faculty of Science and Technology, Keio University, 3-14-1 Hiyoshi, Kohoku-ku, Yokohama 223-8522, Japan. E-mail: hiroaki@applc.keio.ac.jp

cification were obtained using samples from an adult *Lamna ditropis* individual because immature teeth were easily recovered.

Although the ordered structures of the outer layer—consisting of parallel bundles (PBs), radial bundles (RBs), and circumferential bundles (CBs)—have been reported in previous articles,[20,33,36] the complex design of the enameloid—including the construction modes—has not been clarified sufficiently. Here, we focused on the orthogonal configuration of RBs and PBs in the outer layer. In the first section, the detailed architecture consisting of RBs and PBs was revealed from the multidirectional characterization of mature teeth. In the second section, we studied the construction processes of various bundled structures using immure teeth. Differences in the organic matrix and the formation mechanism were found between PBs and RBs. The dual-mode construction of fibrous crystal bundles is deduced to be based on the orthogonal design of the sophisticated architecture consisting of oriented bundles. Moreover, in the third section, we characterized the total design and mechanical properties of the enameloid including the shiny layer, CBs in the outer layer, tangled bundles in the inner layer, and crossed bundles in the ridge/cutting edge layer (RCEL). Finally, our results provide a hint for the future design of biomimetic devices consisting of common phosphate crystals.

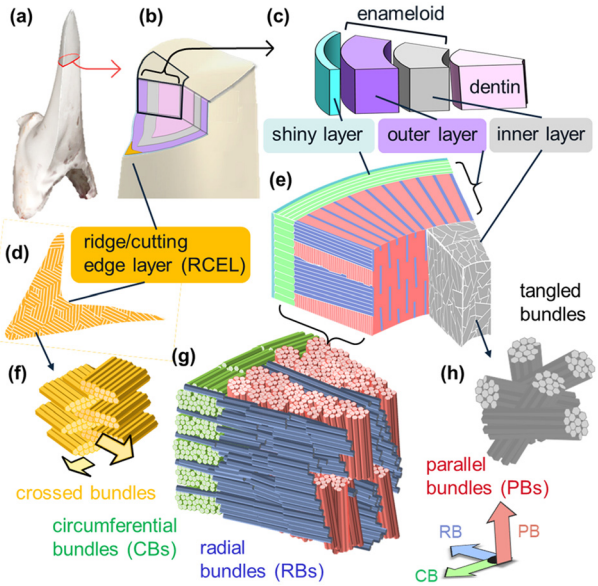

Fig. 1 Schematic illustration of the total architecture of the tooth enameloid of sharks in the Lamnidae family. (a) Appearance and (b) cross-section of a whole tooth, (c) the overall structure of the enameloid, (d) the ridge/cutting edge layer (RCEL), and enlarged images of (f) the RCEL, (g) the outer layer, and (h) the inner layer. Red, blue, green, and yellow arrows indicate the *c*-direction of the rods in PBs, RBs, CBs, and RCEL, respectively.

Results and discussion

Characterization of the orthogonal configuration of FA bundles

Fig. 1 shows a schematic illustration of the hierarchical architecture of the tooth enameloid of sharks in the Lamnidae family. Here, we clarified the structural variation in the bundled design with the multidirectional characterization of various parts of the enameloid (Fig. 1a and b). Previous studies[20,33,36] have shown that the microstructures of the enameloid were classified into four layers: the shiny layer, the outer layer, the inner layer, and the ridge/cutting edge layer (RCEL). It was found that the shiny layer had a random structure, the outer layer an orthogonal structure, and the inner layer a woven structure. Our new findings include the three-dimensional orthogonal structure of the outer layer (Fig. 1c, e and g), the microstructure of the edge layer (Fig. 1d and f), and the structural relationships between the layers. In order to analyze the formation process in the next section, it was important to analyze in detail each layer's microstructure, especially the details of the orthogonal structure of the outer layer.

The enameloid is predominantly composed of fibrous crystals that are assigned to FA elongated along the *c*-axis using SAED patterns (Fig. S2 in the SI) and the fluorine content of ~3–4 atom%.[37] The outer layer, which is the main part of the enameloid, is composed of three bundled structures (PBs, RBs, and CBs) of fibrous FA arranged along three orthogonal directions (Fig. 1g).[20,33,38] We confirmed that all parts of the enameloid are comprised of FA from Raman spectra (Fig. S3 in the SI). Based on X-ray diffraction, TEM images, and compositional analysis, previous works[20,33,36] on shark enemelloid concluded that the main component is FA. The apatite crystal is partially substituted with carbonate groups (B-type substitution) and hydroxyl groups, as confirmed by the shift of the Raman signal of phosphoric acid in the apatite. Since the main purpose of our work is to understand the hierarchical architecture consisting of apatite bundles and its formation process, the apatite rods are represented here as FA.

In the first section, we focused on the orthogonal configuration of the RBs and PBs as the main part of the outer layer (Fig. 1e and g). The ordered bundles consist of fibrous FA 30–80 nm (average 55 nm) wide as shown in Fig. 2. From the horizontal and vertical views of the outer layer, platy bands that form walls from the dentin to the tooth surface were observed to be composed of RBs. The thickness and width of the plates were estimated to be 1–2 μm (Fig. 2b and d) and 20–30 μm (Fig. 2c and d), respectively. Enlarged SEM (Fig. 2b2 and d2) and TEM (Fig. 2b3) images indicate the orthogonal configurations of the RBs and PBs. The PBs occupy ~90 vol% of the outer layer and are arranged perpendicularly to the RBs. We found that PBs and RBs are not directly attached to each other at the boundary (Fig. S4b5 in the SI). This suggests that both bundled structures are produced independently.

Dual-mode construction of oriented FA bundles

We studied the calcification processes of the enameloid by analyzing immature teeth (Fig. S1 in the SI). The maturity of immature teeth increases toward the front surface of the body.

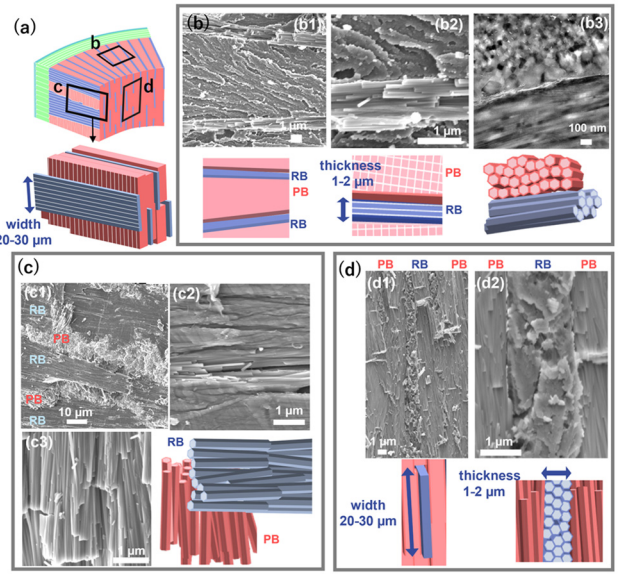

Fig. 2 Schematic illustrations and SEM images of the orthogonal configuration of RBs and PBs in the outer layer. (a) Schematic illustrations of the outer layer and platy bands of RBs with PBs, (b) horizontal and (c, d) vertical SEM views of RBs and PBs in (a). (b3) A TEM image of a section of an FIB-cut plate. Red and blue rods indicate PBs and RBs, respectively. Detailed SEM images are shown in Fig. S4 in the SI.

We used immature teeth located at various positions from the front because these textures were not perfectly calcified under the construction of the enameloid. Since the inorganic contents of the enameloid steeply increase from the 7th position to 5th, the characterization of the 6th and 7th positions is instructive for discussing the calcification mechanism of the enameloid.

Fig. 3b and Fig. S5a in the SI show variations of the calcium/carbon (Ca/C) molar ratio and the chemical composition, respectively, from the enameloid at the base to the tip of an immature tooth as evaluated by energy-dispersive X-ray spectroscopy (EDS). As the Ca/C ratio increases with decrements of carbon and nitrogen and increments of calcium, phosphorus, and fluorine from the base to the tip, the calcification process proceeds from the tip to the base. Here, we categorized the maturation process of the enameloid into four stages: matrix formation before calcification (stage 0), calcification of PBs from non-collagenous fibrils (stage 1), calcification of RBs with collagen fibrils (stage 2), and widening of FA fibers of RBs with a decrease in organic matter (stage 3). Fig. S6 in the SI shows TEM images and a schematic illustration of the matrix formation in stage 0. The change in the infrared (IR) absorption spectra is shown in Fig. S5b in the SI. The presence of signals assigned to the amide groups in stage 0 suggests that the organic matter is mainly composed of proteins. An increase in the signal intensity due to PO_4^{3-} indicates the process of calcification with the growth of apatite crystals. Interestingly, crystal growth proceeds earlier in PBs than in RBs. This suggests that the formation mechanisms and precursor organic matrices of both structures are different regardless

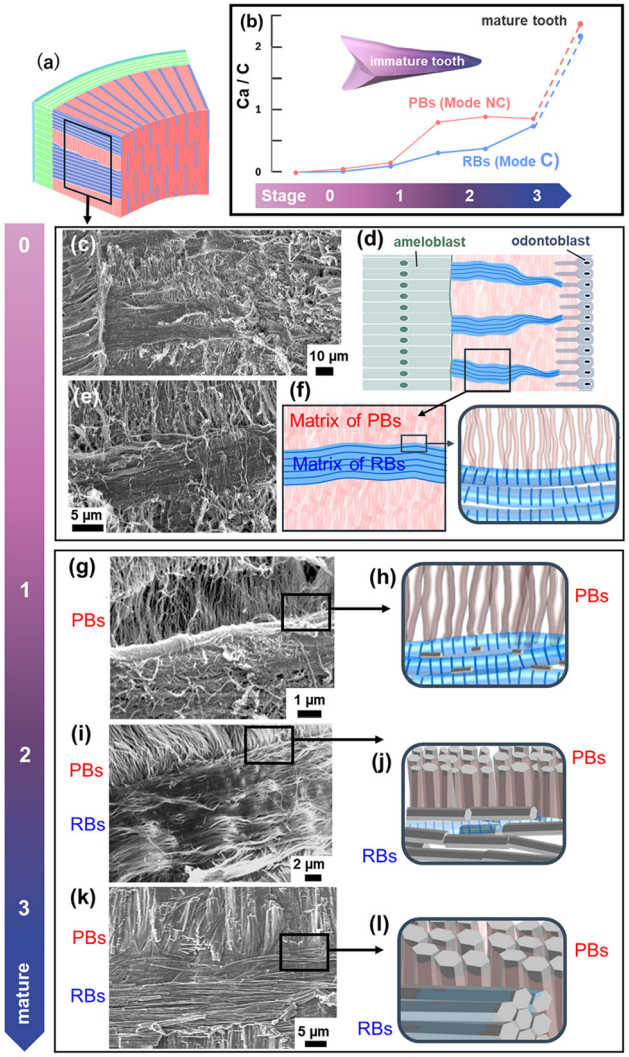

Fig. 3 (a) Overview of the outer layer, (b) variation in the Ca/C ratios of an immature tooth, (c, e, g, i, k) SEM images and (d, f, h, j, l) schematic illustrations of vertical cross-sections of the outer layer (RBs and PBs) at various stages of calcification. (c–f) Stage 0, (g, h) stage 1, (i, j) stage 2, and (k, l) stage 3. Details of PBs and RBs are shown in Fig. 4 and 5, respectively.

of the similarities in the resultant bundled structures. Here, we conclude that PBs and RBs are constructed in the organic matrix through different modes, Mode NC and Mode C, respectively. Details are discussed in the next section.

Schematic illustrations and SEM images shown in Fig. 3c–l clarify the maturation process of the enameloid. Basically, the organic matrix is initially formed between ameloblasts and odontoblasts before calcification (Fig. S6 in the SI). In the initial stage of matrix formation (stage 0), we observed collagen fibrils as black bands between the ameloblasts at the tooth surface and odontoblasts. The formation of collagen fibrils was confirmed by the specific band having a period of 20 nm (Fig. S6c in the SI) and by their composition (C: 86%, N: 8%). At the end of stage 0, collagen bundles 10–30 μm wide bridged from the ameloblasts to the odontoblasts (Fig. 3c–f).

We also found organic fibrils moderately arranged perpendicular to the collagen bundles (Fig. 3e and f). The specific band was not observed on the fibrils (Fig. S6d in the SI) although their composition was almost the same as that of collagen. Thus, the vertical organic structure was deduced to be non-collagenous protein fibrils. The presence of the non-collagenous protein was reported in previous works.[39,40] In mature teeth, we observed that the structure of RBs and PBs was similar to that of the organic matrix (Fig. 3k and l). From these results, the orthogonal configuration was deduced to be constructed by the collagen bundles and the non-collagenous protein fibrils before the enameloid was clarified.

Through the total process from stage 0 to stage 3, PBs consisting of FA rods are formed through the calcification of non-collagenous protein fibrils (Mode NC). Fig. 4 shows schematic illustrations and enlarged SEM and TEM images of the cross-sections of PBs at various stages. As shown in Fig. 3e–h, non-collagenous protein fibrils are formed in the region of the PBs at the end of stage 0. Here we found organic fibrils 4–5 nm wide with bundles (Fig. 4a–c) containing small amounts of calcium and phosphorus. In the early part of stage 1, lattice stripes assigned to FA appeared in protein fibrils with increasing calcium and phosphorus concentrations (Fig. 4d–g). In the late part of stage 1, we observed bundles of straight fiber assigned to *c*-axis elongated FA from their lattice stripes (Fig. 4h–k). The fiber width increased to ~20–50 nm through the attachment of thin crystals (Fig. 4d–k) or the widening of FA crystals preceding calcification from stages 2 to 3 (Fig. 4l–q). Therefore, FA fibers in the RBs were deduced to be produced by the gradual transformation of non-collagenous organic fibrils with the infiltration of calcium and phosphate ions (Fig. S7 in the SI). The organic matter decreases without a change in the rod width in stages 2 and 3 in the PBs. We confirmed the decrease in proteins in stage 2 from a change in the signal intensity of amide groups in the IR spectra (Fig. S6 in the SI) and a decrement of carbon and nitrogen (Fig. S5a in the SI). Here, the formation of PBs from non-collagenous protein fibrils is called "Mode NC". Many lamellar structures that suggest the presence of hydrolytic enzymes[41,42] were found in stages 2 and 3 (Fig. S8 in the SI). Thus, the decrease in organic matter is ascribed to the degradation of the matrix proteins with the enzymes.

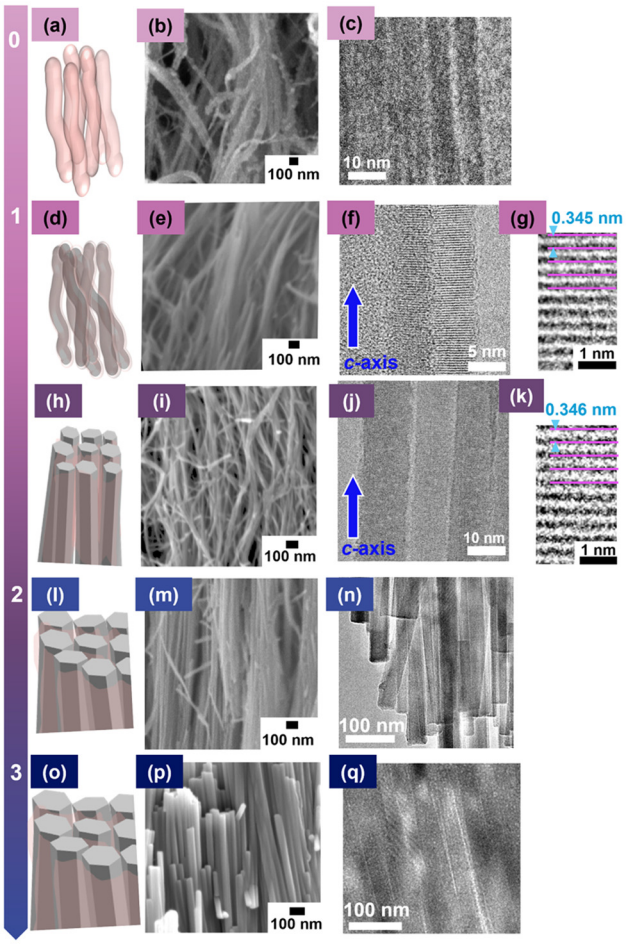

Fig. 4 (a, d, h, l, o) Schematic illustrations and (b, e, i, m, p) enlarged SEM and (c, f, g, j, k, n, q) TEM images of cross-sections of PBs at various stages of Mode NC; (a–c) stage 0, (d–g) the early part of stage 1, (h–k) the late part of stage 1, (l–n) stage 2, (o–q) stage 3. (g, k) Lattice images for (f) and (j), respectively, were assigned to (002) of FA. The rods formed in stage 1 are elongated in the *c*-direction. From stage 2 (l–n) to 3 (o–q), the FA rods thickened. This suggests that the widening of FA rods could occur through the attachment of thin crystals aligned in similar orientations.

Self-organized ribbons of non-collagenous proteins, such as amelogenin, were reported to change into apatite crystals through gradual transformation.[43–46] Unfortunately, this study has not revealed details of the organic and inorganic structures. Further investigation is needed for clarification.

Through the total process from stage 0 to stage 3, RBs consisting of FA rods are formed through the calcification of the collagen fibrils. We call the formation of RBs from collagen bundles "Mode C". Fig. 5 shows schematic illustrations and SEM and TEM images of the cross-sections of RBs at various stages. As shown in Fig. 3c–f, we observed collagen bundles 10–30 μm wide and over several hundred micrometers long in stage 0. Here, we focus on the calcification of collagen fibrils that show a specific band (Fig. 5a–c) and contain small amounts of calcium and phosphorus. In stage 1, tiny rods 5–7 nm long were attached around collagen fibrils having the specific band (Fig. 5d–f). In the early part of stage 2, the number of rods 10–15 nm wide surrounding the fibrils increased with decreasing organic matter (Fig. 5g and h). The SAED pattern indicates that the rods are FA elongated in the *c*-direction. Here, the widening of rods is inferred to occur through the attachment of thin crystals (Fig. 5g–i). The decrease in proteins in stage 2 was suggested by a change in the signal intensity of amide groups in the IR spectra (Fig. S5b in the SI) and the decrement of carbon and nitrogen (Fig. S5a in the SI). In the late part of stage 2, the widening of rod-like crystals was observed in the absence of collagen fibrils (Fig. 5j–l). Finally, the FA rods in RBs are produced by crystal growth of *c*-axis-oriented FAs along with collagen fibrils that disappear in stage 3 (Fig. 5m–o).

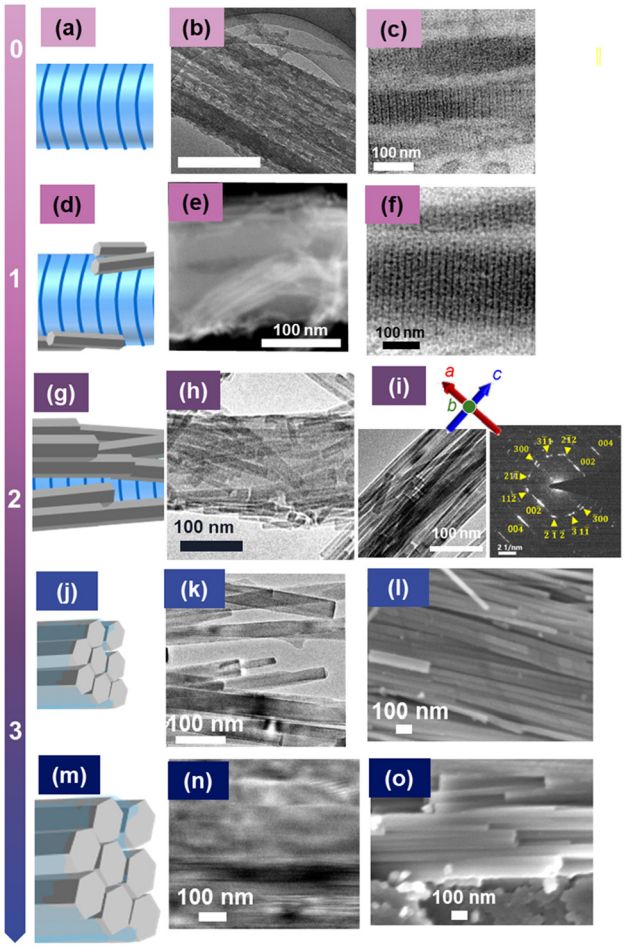

Fig. 5 (a, d, g, j, m) Schematic illustrations and (b, c, e, f, h, i, k, n) TEM images of cross-sections with an SAED pattern and the crystal axis of RBs and (l, m) enlarged SEM at various stages of Mode C; (a–c) stage 0, (d–f) stage 1, (g–i) the early part of stage 2, (j–l) the late part of stage 2, and (m–o) stage 3. (e) An image obtained by high-angle annular dark field scanning TEM.

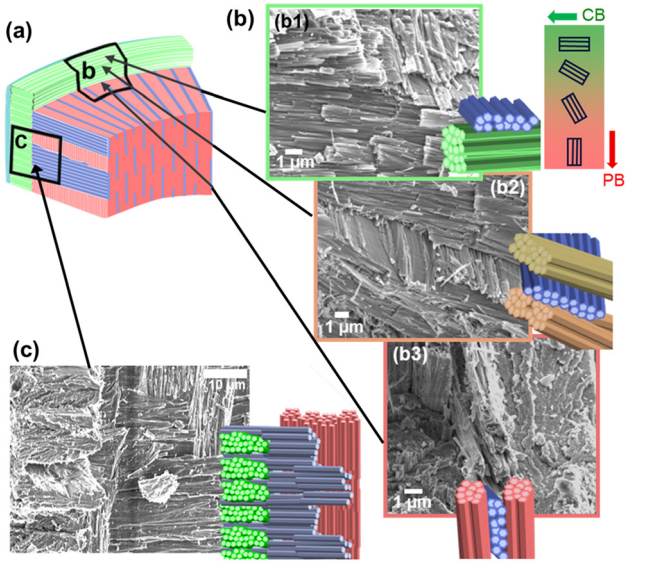

Fig. 6 (a) A schematic illustration of the outer layer and (b, c) SEM images with illustrations of various structures around the CBs. (b) Overviews and (c) vertical views. Red, blue, and green rods indicate PBs, RBs, and CBs, respectively. Khaki and orange rods indicate an intermediate state between PBs and CBs as a coloured map of rod orientation. Details around the CBs are shown in Fig. S9 in the SI.

Previous studies have reported that apatite rods formed along collagen fibrils.[47–49] The alignment of the functional groups of amino acids, such as COO^- or NH_3^+, could induce the nucleation of apatite.[50]

Characterization of the total architecture of FA bundles

As shown in Fig. 1, shark tooth enameloid has a hierarchical architecture consisting of bundled FA crystals. In the first and second sections, the orthogonal configurations of RBs and PBs were revealed with their formation processes. In the third section, we clarified the structural variation of parts other than RBs and PBs, such as the shiny, inner, and ridge/cutting edge layers and CBs in the outer layer (Fig. 1b, d and f, respectively).

In the outer layer, CBs have a circumferential fibrous structure parallel to the surface (Fig. 1e andg). Fig. 6 and Fig. S9 in the SI show the SEM images of various structures around the CBs. As reported in previous articles,[20,33] three bundled structures (PBs, RBs, and CBs) of fibrous FA are arranged along three orthogonal directions (Fig. 6c). However, the alignment of FA was found to be more complicated. From an overview image (Fig. 6b), we see the fiber direction gradually change from the vertical position of PBs (b1) to the horizontal state of the CBs (b3) through the intermediate (b2). Finally, fibers of the CBs seemed to connect to those of the PBs with a twist of the platy bands of the RBs. We confirmed the gradual change in the fiber direction from PBs to CBs with twisting RBs from vertical views (Fig. S9f in the SI). These results suggest that CBs have the same origin as PBs. The twisting region of the outer layer of the front side of a tooth is smaller than that of the rear side.

The inner layer was reported to be composed of tangled FA bundles (Fig. 1c, e and h).[20,33,36,38] Here, we observed the gradual disordering of bundles that are similar to PBs from the boundary of the outer layer to the dentin (Fig. 7a and c). A definite boundary was not observed between the vertical bundles of the PBs and tangled bundles with a width of 1–3 μm (Fig. S10 in the SI). A decrease in the width of the RB bands is a feature of the inner layer (Fig. 7c and d). As mentioned above, collagen bundles as the organic matrix before calcification are essential for the production of the orthogonal configuration of RBs and PBs. Thus, thin RB bands are insufficient for the ordering of vertical bundles of FA fibers.

The bundled FA fibers of the RCEL are different from those of other parts of the enameloid (Fig. 1d and f). However, the structure of the RCEL has not been sufficiently characterized. Fig. 8 shows enlarged SEM images of the crossed bundles on the horizontal cross-sections of the RCEL. The FA bundles having two different directions are stacked upon each other

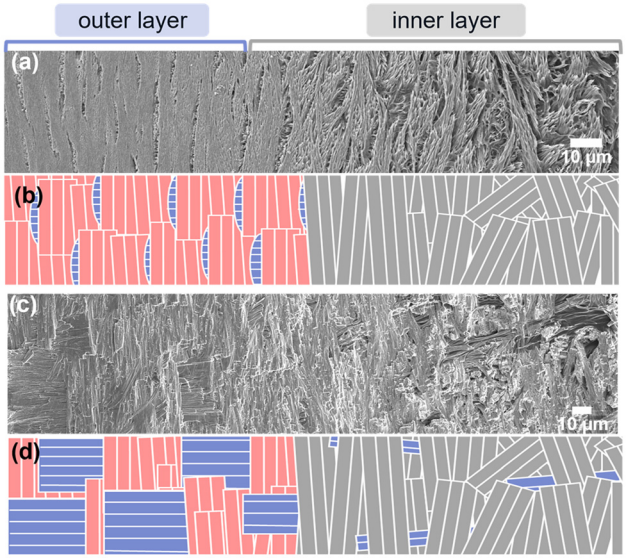

Fig. 7 (a, c) SEM images and (b, d) schematic illustrations of vertical sections of the outer and inner layers. (a, b) Variation of the ordering from PBs to the tangled bundles, and (c, d) variations in the platy bands of RBs.

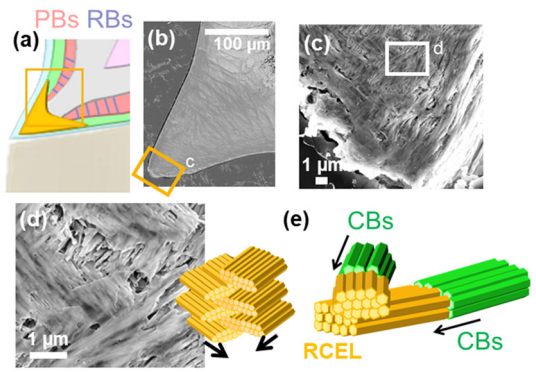

Fig. 8 (a, e) Schematic illustrations and (b–d) SEM image of the crossed bundles in the RCEL on the horizontal section of the edge. The CBs of the front and rear sides are connected with the RCEL without clear boundaries (a, b). FA bundles having two different directions are stacked on each other (c, d, e). Thus, the crossed bundles of the RCEL seemed to be formed through the elongation and intersection of the CBs (e) of the front and rear sides with each other.

(Fig. 8c and d). The hardness of the RCEL was similar to that of the PBs, although its Young's modulus was lower than that of the PBs (Fig. S11 in the SI). These results suggest that the RCEL is hard but bendable due to the cross structure. The crossed bundles of the RCEL seemed to be formed through the stacking of the CBs (Fig. 8e) of the front and rear sides (Fig. S1 in the SI). As mentioned above, the CBs are related to the PBs. Thus, the RCEL is also estimated to be derived from the PBs.

The topmost part is the shiny layer, which is comprised of random assemblies of FA[20,21,33,38] crystals. Details of the microstructure and shape of the crystals were revealed by mild etching with EDTA (Fig. S12 in the SI). Here, we found that the shiny layer is composed of the upper region, consisting of thinner fibrous units 20–50 nm wide, and the lower region, in which thicker fibers 100–200 nm wide are randomly arranged. Moreover, the incursion of RBs connecting the surface was observed in this layer.

Fig. S13 in the SI shows the TEM images of the initial stage of the formation of the outer layer, the inner layer, the RCEL, and the shiny layer. FA fibers in these layers were basically found to originate from the same non-collagenous organic fibrils as in PBs. Therefore, FA bundles in the enameloid are concluded to be produced through two modes of calcification. RBs are constructed from collagen bundles (Mode C), and the other parts—such as the PBs and CBs in the outer layer, the inner layer, and the RCEL—are produced from non-collagenous protein fibrils (Mode NC).

Conclusions

The hierarchical structures of the tooth enameloid of sharks in the Lamnidae family were characterized completely. The orthogonal configuration of radial bundles (RBs) and parallel bundles (PBs) of fluorapatite (FA) in the main part of the enameloid was deduced to be formed through dual-mode construction originating from the calcification of collagen bundles and non-collagenous protein fibrils, respectively. The crystal growth of *c*-axis-oriented FA along with collagen fibrils is essential for the calcification of RBs. FA fibers in PBs, which are arranged perpendicularly to RBs, are formed with the gradual transformation of non-collagenous protein fibrils infiltrated by calcium and phosphate ions. Other parts consisting of FA fibers, such as bundles in the inner and ridge/cutting edge layers, were also deduced to be produced in the non-collagen mode. Our findings are useful for understanding the structural design of the sophisticated architectures of a wide variety of biominerals and the fabrication of biomimetic architectures.

Experimental

Sample collection and preparation

For structural analysis, the tooth enameloid of sharks in the Lamnidae family was obtained from shark jaw specimens purchased on the internet or frozen jaws. Mature teeth were horizontally and vertically fractured with a hammer or cut and polished after an epoxy resin embedding. A thin-film sample about 100 nm thick was cut from a fractured surface of a mature tooth using a focused ion beam (FIB).

For formation process analysis, teeth during enameloid formation were removed from fresh Lamnidae heads. These immature tooth samples were immediately fixed with Karnovsky's fixative (2.5% glutaraldehyde and 2% paraformaldehyde, 0.1 M HEPES buffer, pH 7.4). For critical point drying (Leica CPD300), fixed samples were rinsed with HEPES buffer

(0.1 M, pH 7.4) and dehydrated with ethanol before drying. For ultra-thin sections, fixed samples were post-fixed with 1% osmium tetroxide and rinsed with HEPES buffer (0.1 M, pH 7.4). These samples were dehydrated and Epoxy resin embedded. Ultra-thin sections were cut using an ultramicrotome (Leica UC7) with a diamond knife. Some of the ultra-thin sections were stained with uranyl acetate and lead citrate, OTE.

For TEM observation of CPD samples, the target fragments were picked with a tungsten probe (probe diameter 1 μm) using a micro-manipulator (MicroSupport Axis Pro SS).

Analytical methods

We used a field-emission SEM (JEOL JSM-7600F) operating at 5.0 kV and SEM-EDS operating at 10 kV to observe the meso- and nanostructures of the surface and cross-section of the teeth. The surfaces and cross-sections of fractured samples were etched mildly with a 0.1 M ethylene diamine tetraacetate solution adjusted to pH 7.2 with HCl[51] to remove damaged topmost layers and then coated with osmium for SEM observation. We evaluated the crystal structure and composition of teeth using Raman scattering spectroscopy (Horiba LabRAM HR Evolution) and microscopic reflected infrared spectroscopy (Shimadzu IRAffinity-1, AIM-8800). CPD samples were observed using TEM (FEI Tecnai G2, 200k; Tecnai Osiris, 200 kV) with selected area electron diffraction (SAED) and TEM-EDS. To analyze SAED patterns, electron diffraction simulation software ReciPro was used.[52] Ultra-thin sections were observed using TEM (FEI Tecnai, 120 kV; JEOL JEM-1400Plus, 100 kV; Osiris, 120 kV) and TEM-EDS. 3D scanning images were taken using a Keyence 3D Scanner CMM ControllerVL-700.

Nanoindentation was performed using a KLA iMicro Nanoindenter with a Berkovich indenter tip with a load of 1 mN. The mapping images were obtained from polished surfaces of the mature teeth embedded in epoxy resin.

Author contributions

H. I. supervised the project. S. A., Y. O., and H. I. designed the experimental procedures of structure analysis. S. A. and H. I analyzed the structures of shark enameloids and discussed the results. All authors reviewed the manuscript.

Conflicts of interest

There are no conflicts to declare.

Data availability

The authors declare that the data supporting the findings of this study are available within the paper and its supplementary information (SI). Supplementary information: photos and illustrations of a jaw and teeth of *Isurus oxyrinchus* (Fig. S1); TEM images and SAED patterns of fluorapatite (FA) rods in the enameloid of a mature tooth (Fig. S2); a schematic illustration, an SEM image, and Raman spectra of the enameloid of a mature tooth (Fig. S3); an SEM image of the horizontal fractured section and TEM images of the horizontal FIB section of the PBs and RBs (Fig. S4); variation of the chemical composition and IR spectra of the outer layer of an immature tooth (Fig. S5); a schematic illustration and TEM images and for the matrix formation in stage 0 (Fig. S6); TEM images and an elemental mapping of calcium of thin sections of the PBs at stage 0 (Fig. S7); TEM images of stained ultra-thin sections in the outer layer in stage 3 (Fig. S8); schematic illustrations and SEM images of various structures around the CBs (Fig. S9); SEM images of fractured surfaces of the inner layer and TEM images of the FIB section of the inner layer in a mature tooth (Fig. S10); the hardness and Young's modulus of the enameloid in a mature tooth (Fig. S11); SEM images of the shiny layer (Fig. S12); TEM images of stained ultra-thin sections of the RCEL, the inner layer, and the shiny layer in an immature tooth (Fig. S13). See DOI: **https://doi.org/10.1039/d5nr03589a**.

Raw data files are available from the corresponding author upon reasonable request.

Acknowledgements

This work was supported by JSPS KAKENHI grant number JP21H01627.

References

1 H. P. Yu and Y. J. Zhu, *Chem. Soc. Rev.*, 2024, **53**, 4490–4606.
2 Z. Deng, Z. Jia and L. Li, *Adv. Sci.*, 2022, **9**, 1–32.
3 J. W. C. Dunlop and P. Fratzl, *Annu. Rev. Mater. Res.*, 2010, **40**, 1–24.
4 U. G. K. Wegst, H. Bai, E. Saiz, A. P. Tomsia and R. O. Ritchie, *Nat. Mater.*, 2015, **14**, 23–36.
5 H. Cölfen and S. Mann, *Angew. Chem., Int. Ed.*, 2003, **42**, 2350–2365.
6 E. Seknazi and B. Pokroy, *Adv. Mater.*, 2018, **30**, 1–6.
7 M. Suzuki, *Biosci. Biotechnol. Biochem.*, 2020, **84**, 1529–1540.
8 Y. Oaki and H. Imai, *Adv. Funct. Mater.*, 2005, **15**, 1407–1414.
9 Y. Oaki, A. Kotachi, T. Miura and H. Imai, *Adv. Funct. Mater.*, 2006, **16**, 1633–1639.
10 A. Velasco-Hogan, J. Xu and M. A. Meyers, *Adv. Mater.*, 2018, **30**, 1800940.
11 W. Huang, D. Restrepo, J. Y. Jung, F. Y. Su, Z. Liu, R. O. Ritchie, J. McKittrick, P. Zavattieri and D. Kisailus, *Adv. Mater.*, 2019, **31**, 1–37.
12 D. Nepal, S. Kang, K. M. Adstedt, K. Kanhaiya, M. R. Bockstaller, L. C. Brinson, M. J. Buehler, P. V. Coveney, K. Dayal, J. A. El-Awady, L. C. Henderson, D. L. Kaplan, S. Keten, N. A. Kotov, G. C. Schatz,

S. Vignolini, F. Vollrath, Y. Wang, B. I. Yakobson, V. V. Tsukruk and H. Heinz, *Nat. Mater.*, 2023, **22**, 18–35.
13 J. Wilmers and S. Bargmann, *Acta Biomater.*, 2020, **107**, 1–24.
14 K. A. Selvig, *J. Ultrastruct. Res.*, 1972, **41**, 369–375.
15 C. A. Stifler, J. E. Jakes, J. D. North, D. R. Green, J. C. Weaver and P. U. P. A. Gilbert, *Acta Biomater.*, 2021, **120**, 124–134.
16 M. Hegedűs, V. K. Kis, Á. Szabó, I. Kovács, N. Rózsa and Z. Kovács, *Mater. Des.*, 2023, **234**, 112369.
17 A. Koblischka-Veneva, M. R. Koblischka, J. Schmauch and M. Hannig, *Nano Res.*, 2018, **11**, 3911–3921.
18 Z. Deng, H. C. Loh, Z. Jia, C. A. Stifler, A. Masic, P. U. P. A. Gilbert, R. Shahar and L. Li, *Acta Biomater.*, 2022, **137**, 147–161.
19 J. Enax, O. Prymak, D. Raabe and M. Epple, *J. Struct. Biol.*, 2012, **178**, 290–299.
20 J. Enax, A. M. Janus, D. Raabe, M. Epple and H. O. Fabritius, *Acta Biomater.*, 2014, **10**, 3959–3968.
21 S. Amini, H. Razi, R. Seidel, D. Werner, W. T. White, J. C. Weaver, M. N. Dean and P. Fratzl, *Nat. Commun.*, 2020, **11**, 5971.
22 M. Goto, *Kokubyo Gakkai Zasshi*, 1978, **45**, 527–584.
23 B. Berkovitz and P. Shellis, *The Teeth of Non-Mammalian Vertebrates*, Elsevier Science and Technology, 2016, pp. 311–330.
24 R. S. Lacruz, S. Habelitz, J. T. Wright and M. L. Paine, *Physiol. Rev.*, 2017, **97**, 939–993.
25 C. A. Stifler, J. E. Jakes, J. D. North, D. R. Green, J. C. Weaver and P. U. P. A. Gilbert, *Acta Biomater.*, 2021, **120**, 124–134.
26 E. Kallenbach, *Cell Tissue Res.*, 1986, **246**, 455–461.
27 I. Sasagawa, *J. Anat.*, 1989, **164**, 175–187.
28 I. Sasagawa, *Microsc. Res. Tech.*, 2002, **59**, 396–407.
29 N. E. Kemp and J. H. Park, *Arch. Oral Biol.*, 1974, **19**, 633–644.
30 Y. Miake, T. Aoba, E. C. Moreno, S. Shimoda, K. Prostak and S. Suga, *Calcif. Tissue Int.*, 1991, **48**, 204–217.
31 E. E. Graham, *J. Exp. Zool.*, 1985, **234**, 185–191.
32 P. G. Satchell, X. Anderton, O. H. Ryu, X. Luan, A. J. Ortega, R. Opamen, B. J. Berman, D. E. Witherspoon, J. L. Gutmann, A. Yamane, M. Zeichner-David, J. P. Simmer, C. F. Shuler and T. G. H. Diekwisch, *J. Exp. Zool.*, 2002, **294**, 91–106.
33 J. Wilmers, M. Waldron and S. Bargmann, *Nanomaterials*, 2021, **11**, 969.
34 J. P. Correia, *Zoo Biol.*, 1999, **18**, 313–317.
35 H. Botella, J. I. Valenzuela-Ríos and C. Martínez-Perez, *Lethaia*, 2009, **42**, 365–376.
36 C. Fellah, T. Douillard, E. Maire, S. Meille, B. Reynard and G. Cuny, *J. Struct. Biol.*, 2021, **213**, 107664.
37 C. Chen, Z. Wang, M. Saito, T. Tohei, Y. Takano and Y. Ikuhara, *Angew. Chem., Int. Ed.*, 2014, **53**, 1543–1547.
38 G. Cuny and S. Risnes, *PalArch's J. Vertebr. Palaeontol.*, 2005, **3**, 8–19.
39 E. E. Graham, *J. Exp. Zool.*, 1985, **234**, 185–191.
40 P. G. Satchell, X. Anderton, O. H. Ryu, X. Luan, A. J. Ortega, R. Opamen, B. J. Berman, D. E. Witherspoon, J. L. Gutmann, A. Yamane, M. Zeichner-David, J. P. Simmer, C. F. Shuler and T. G. H. Diekwisch, *J. Exp. Zool.*, 2002, **294**, 91–106.
41 S. Shulenin, L. M. Nogee, T. Annilo, S. E. Wert, J. A. Whitsett and M. Dean, *N. Engl. J. Med.*, 2004, **350**, 1296–1303.
42 G. K. Menon, R. Ghadially, M. L. Williams and P. M. Elias, *Br. J. Dermatol.*, 1992, **126**, 337–345.
43 O. Martinez-Avila, S. Wu, S. J. Kim, Y. Cheng, F. Khan, R. Samudrala, A. Sali, J. A. Horst and S. Habelitz, *Biomacromolecules*, 2012, **13**, 3494–3502.
44 K. M. M. Carneiro, H. Zhai, L. Zhu, J. A. Horst, M. Sitlin, M. Nguyen, M. Wagner, C. Simpliciano, M. Milder, C. L. Chen, P. Ashby, J. Bonde, W. Li and S. Habelitz, *Sci. Rep.*, 2016, **6**, 1–11.
45 Y. Bai, Z. Yu, L. Ackerman, Y. Zhang, J. Bonde, W. Li, Y. Cheng and S. Habelitz, *Proc. Natl. Acad. Sci. U. S. A.*, 2020, **117**, 19201–19208.
46 E. Kallenbach, *Cell Tissue Res.*, 1986, **246**, 455–461.
47 C. Hu, M. Zilm and M. Wei, *J. Biomed. Mater. Res., Part A*, 2016, **104**, 1153–1161.
48 Y. Qi, Z. Ye, A. Fok, B. N. Holmes, M. Espanol, M. P. Ginebra and C. Aparicio, *ACS Biomater. Sci. Eng.*, 2018, **4**, 2755–2766.
49 F. Nudelman, K. Pieterse, A. George, P. H. H. Bomans, H. Friedrich, L. J. Brylka, P. A. J. Hilbers, G. De With and N. A. J. M. Sommerdijk, *Nat. Mater.*, 2010, **9**, 1004–1009.
50 M. Tanahashi and T. Matsuda, *J. Biomed. Mater. Res.*, 1997, **34**, 305–315.
51 C. P. Lin, W. H. Douglas and S. L. Erlandsen, *J. Histochem. Cytochem.*, 1993, **41**, 381–388.
52 Y. Seto and M. Ohtsuka, *J. Appl. Crystallogr.*, 2022, **55**, 397–410.

